Supplementary Information for

Label-free detection of single nanoparticles and biological molecules using microtoroid optical resonators

J. Su, A.F.G. Goldberg, and B.M. Stoltz

Time in between binding events is faster than from diffusion alone

The arrival rate of particles to the vicinity of the toroid = $C\hat{Q}$, where *C* is the concentration (number of particles/volume), and $\hat{Q}$ is the injection flow rate (volume/time). Given a concentration of 150 aM and an injection rate of 1 mL min^{-1}, this gives an arrival rate of 1500 particles per second. The velocity, *V*, from injection is given by, $V = \frac{\hat{Q}}{A}$, where A is the cross-sectional area of the inlet tube. *V* is therefore 550 mm per second. From here we calculate a Reynolds number of 550, meaning convection is 550 times bigger than viscous diffusion of the liquid molecules. The frequency, *f*, of vortex shedding over the toroid is given by $f = V/h$, where h = 0.1 mm (**Supplementary Fig. S2**), therefore an encounter rate of 10^3 to 10^4 Hz seems feasible. As smaller particles tend to be influenced by smaller vortices more, vortices shed from the ~500 nm diameter optical fiber may play a role, making the encounter rate even higher. However, the highly nonlinear flow process under stopped flow conditions is known to be complicated. A further analysis will be needed to resolve the mechanism of fast binding in small scale flow.

Noise determination

In our experiments, we establish our noise level by measuring how the resonance wavelength of the microtoroid changes over time when it is immersed in a buffer (background) solution. The reason we calculate our noise level in this manner is because our particle detection experiments are performed in buffer solutions, so measuring how the resonance wavelength of the microtoroid changes in just a buffer solution represents our control case of what the resonance shift looks like when there are no particles.

We calculate our noise levels before and after feedback control by calculating the standard deviation of the resonance wavelength value after subtracting a general trend (see below). Before feedback control, the standard deviation of the resonance wavelength value over 60 seconds is ~ 1 pm (**Fig.2a**). After enabling feedback control, the fluctuations are significantly decreased to ~ 0.07 fm over 10 seconds (**Fig. 2b**). The shorter time interval over which we average our signal in the frequency locking case reflects the higher data acquisition rate that is enabled with feedback control.

If we calculate the noise level (standard deviation) over 1 ms intervals which is the approximate time between binding events for our r=2.5 nm nanoparticle experiments, this number reduces further to $\sim 9.6 \times 10^{-4}$ fm. This represents an average over 20 data points for 10,000 intervals. We note that the noise level decreases when averaging over smaller time intervals as our noise is not white noise. Before these numbers are calculated, we first computationally filter the data to remove known sources of noise and then apply a median filter of window size 1001. For example, using this method of calculating noise levels, along with measurements of maximum step size, we determine that our SNR for IL-2 in the experiment shown in Fig. 5d is 5.2 and our SNR for the 10 nm radius nanoparticles shown in Fig. 4c is 35.

A general trend was subtracted from the buffer data before computing noise levels to account for thermal drift of the system. Due to the large circulating intensities within optical resonators, there is a significant, but slow (on the order of seconds), thermal drift of the resonance frequency over time. This is due to index of refraction changes due to temperature changes which have been established to be ~1 pm/1°C in silica. Thermal drift may also occur due to temperature fluctuations in the room and is considered to be one of the main sources of environmental noise for optical resonators. We expect thermal drift as we are not working in a temperature controlled environment and it is reasonable to expect temperature changes of 1–2 degrees. A downward drift indicates cooling whereas an upwards drift indicates heating of the microtoroid. We note that this long term overall drift is large (> fm) compared to the wavelength shift we expect to see from a single molecule which is 0.005 fm. In addition, we also note that the time scale of the long term shift due to temperature is on the order of seconds while the time scale of a single molecule binding event is on the order of milliseconds, and therefore, this thermal drift does not hamper our ability to detect individual binding events.

Linker Synthesis

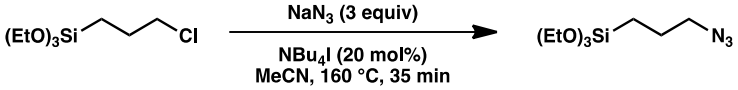

3-azidopropyltriethoxysilane. Two flame-dried, 20 mL microwave vials were each charged with 3-chloropropyltriethoxysilane (1.0 mL, 4 mmol, 1 equiv), sodium azide (813.8 mg, 12 mmol, 3 equiv), tetrabutylammonium iodide (310.6 mg, 0.84 mmol, 0.2 equiv) and dry acetonitrile (20 mL). The vials were sequentially heated in a Biotage Initiator microwave (160 °C) for 35 minutes. The reaction mixtures were combined and the solvent was removed in vacuo. To the residue was added pentane, and the mixture was filtered through Celite then concentrated in vacuo. The crude product (1.5439 g, 75% yield) appeared clean by NMR, but could be further purified by Kugelrohr distillation (0.1–0.3 torr, 88 °C bath temperature) to afford a colorless oil: ^{1}H NMR (300 MHz, $CDCl_3$) δ 3.82 (q, J = 7.0 Hz, 4H), 3.27 (t, J = 7.0 Hz, 2H), 1.79 – 1.64 (m, 2H), 1.23 (t, J = 7.0 Hz, 9H), 0.75 – 0.60 (m, 2H).

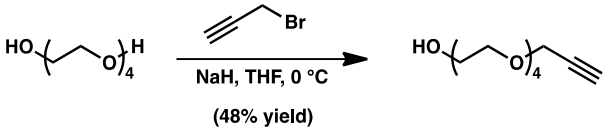

HO–TEG–Alkyne. A flame-dried 1 L round-bottom flask, equipped with a magnetic stir-bar was charged with sodium hydride (1.5070 g, 60% in mineral oil, 37 mmol, 1.2 equiv) then sealed with a rubber septum under nitrogen. To the flask was added THF (ca. 400 mL) via cannula, then the reaction mixture was cooled in an ice-water bath. Tetraethyleneglycol (8.0 mL, 46 mmol, 1.5 equiv) was added dropwise to afford a homogeneous mixture. To the stirring mixture was added propargyl bromide (3.4 mL, 80 wt% in toluene, 31 mmol, 1 equiv) dropwise, and the resulting solution was stirred until complete consumption of the bromide was observed by thin layer

chromatography (2.5 hours). The reaction was quenched by addition of saturated ammonium chloride and water and the bulk of the THF was removed by rotary evaporation. The resulting mixture was extracted with dichloromethane (75 mL x 4) and the combined organic fractions were dried over anhydrous magnesium sulfate, clarified with activated charcoal, filtered and concentrated in vacuo. The residue was purified by flash chromatography (20:1 DCM:MeOH) to afford the desired propargyl ether (3.5388 g, 48% yield): ^{1}H NMR (300 MHz, $CDCl_3$) δ 4.20 (d, J = 2.4 Hz, 2H), 3.75 – 3.63 (m, 14H), 3.63 – 3.58 (m, 2H), 2.65 (t, J = 6.0 Hz, 1H), 2.42 (t, J = 2.4 Hz, 1H).

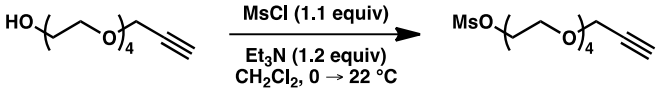

MsO–TEG–Alkyne. A flame-dried round-bottom flask was equipped with a magnetic stir-bar and charged with HO–TEG–Alkyne (3.4418 g, 14.8 mmol, 1 equiv). The flask was sealed with a rubber septum under nitrogen. To the flask was added dichloromethane (75 mL) and freshly distilled triethylamine (2.48 mL, 17.8 mmol, 1.2 equiv). The flask was then cooled in an ice-water bath, and mesyl chloride (1.26 mL, 16.3 mmol, 1.1 equiv) was added dropwise to the stirring mixture. Consumption of the starting material was observed by thin layer chromatography after 15 minutes, and saturated aqueous ammonium chloride was added then the phases were separated. The aqueous layer was extracted with additional dichloromethane (100 mL x3), then the combined organic layers were dried over magnesium sulfate, filtered, and concentrated in vacuo. The residue was purified by flash chromatography (40:1 DCM:MeOH) to afford the desired mesylate in a quantitative yield: ^{1}H NMR (300 MHz, Chloroform-*d*) δ 4.43 – 4.33 (m, 2H), 4.20 (d, J = 2.4 Hz, 2H), 3.81 – 3.73 (m, 2H), 3.73 – 3.60 (m, 12H), 3.08 (s, 3H), 2.43 (t, J = 2.4 Hz, 1H).

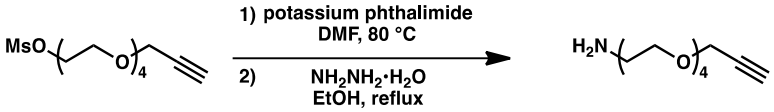

H_2N–TEG–Alkyne. A flame-dried 50 mL round-bottom flask was charged with MsO–TEG–Alkyne (1.0082 g, 3.2 mmol, 1 equiv) and sealed with a rubber septum under nitrogen. Dry DMF (13.5 mL) was added by syringe, followed by rapid addition of potassium phthalimide (720.8 mg, 3.9 mmol, 1.2 equiv). The thick slurry was heated in an 80 °C oil bath with good stirring. After 3 hours, additional potassium phthalimide (380 mg, 2.0 mmol) was added to the mixture, and heating was continued overnight. The reaction mixture was partitioned between dichloromethane and water and the phases were separated. The aqueous layer was extracted exhaustively with dichloromethane (until no product remained in the aqueous layer). The combined organics were dried over magnesium sulfate, filtered and concentrated in vacuo. The residue was purified by flash chromatography (40:1 DCM:MeOH) to afford a white crystalline solid that was carried forward in its entirety to the next stage. A round-bottom flask was charged with the phthalimide product from the previous stage, hydrazine hydrate (473 µL, 9.74 mmol, 3 equiv), and absolute ethanol (32 mL). The flask was equipped with a stir bar and a reflux condenser. The mixture was heated to reflux with stirring for an hour, at which point complete consumption of the starting

material was observed by thin layer chromatography. The reaction mixture was filtered to remove the white precipitate formed in the reaction and the filtrate was concentrated in vacuo. The residue was dry-loaded onto silica gel and purified by column chromatography (40:1 DCM:MeOH → 15:1:0.05 DCM:MeOH:$NH_4OH_{(aq)}$ → 10:1:0.05 DCM:MeOH:$NH_4OH_{(aq)}$) to afford the primary amine (616.0 mg, 82% yield over two steps) as a yellowish oil: ^{1}H NMR (300 MHz, $CDCl_3$) δ 4.23 – 4.12 (m, 2H), 3.75 – 3.56 (m, 14H), 3.55 – 3.44 (m, 2H), 2.91 – 2.79 (m, 2H), 2.46 – 2.39 (m, 1H), 1.84 (s, 2H).

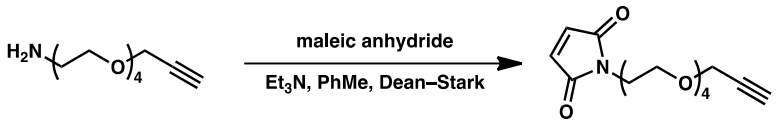

MAL–TEG–Alkyne. A round-bottom flask was charged with H_2N–TEG–Alkyne (231 mg, 1 mmol, 1 equiv), maleic anhydride (107.7 mg, 6.5 mmol, 1.1 equiv), triethylamine (14 μL, 0.1 mmol, 0.1 equiv), and toluene (30 mL). The flask was fitted with a Dean–Stark trap and a reflux condenser, then heated to vigorous reflux for 36 h. The reaction mixture was concentrated in vacuo and dissolved in dichloromethane (60 mL). This solution was washed with aqueous hydrochloric acid (0.1 N) then brine. The organic layer was dried over anhydrous magnesium sulfate, filtered, and concentrated in vacuo. The residue was purified by column chromatography (40:1 DCM:MeOH) to afford the maleimide (42.0 mg, 14% yield): ^{1}H NMR (300 MHz, $CDCl_3$) δ 6.70 (s, 2H), 4.20 (d, J = 2.4 Hz, 2H), 3.76 – 3.58 (m, 16H), 2.43 (t, J = 2.4 Hz, 1H), 1.62 (s, 2H).

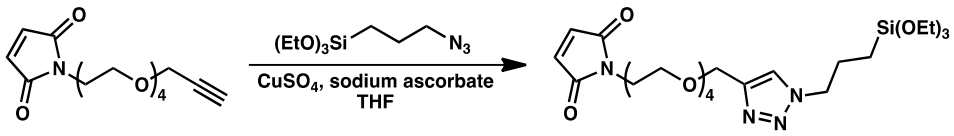

MAL–TEG–Si. A 4 mL vial was charged with MAL–TEG–Alkyne (35.0 mg, 0.11 mmol, 1 equiv) and THF (1 mL). To the solution was added 3-azidopropyltriethoxysilane (27.8 mg, 0.11 mmol. 1 equiv) and sodium ascorbate (13.4 mg, 0.068 mmol, 0.5 equiv). Finally, copper (II) sulfate (11 μL, 1M in H_2O, 0.011 mmol, 0.1 equiv) was added and a brown precipitate was immediately observed. After 30 minutes, additional copper (II) sulfate (22 μL) was added, and the suspension was stirred overnight. The reaction mixture was partitioned between dichloromethane and brine, and the phases were separated. The aqueous phase was further extracted with dichloromethane (15 mL x 3). The combined organics were dried over magnesium sulfate, filtered and concentrated in vacuo. The residue was purified by flash chromatography (20:1 DCM:MeOH) to afford the desired triazole (39.4 mg, 63% yield): ^{1}H NMR (300 MHz, $CDCl_3$) δ 7.56 (s, 1H), 6.67 (s, 2H), 4.65 (s, 2H), 4.31 (t, J = 7.2 Hz, 2H), 3.78 (q, J = 7.0 Hz, 6H), 3.71 – 3.51 (m, 16H), 2.07 – 1.91 (m, 2H), 1.18 (t, J = 7.0 Hz, 9H), 0.64 – 0.50 (m, 2H).

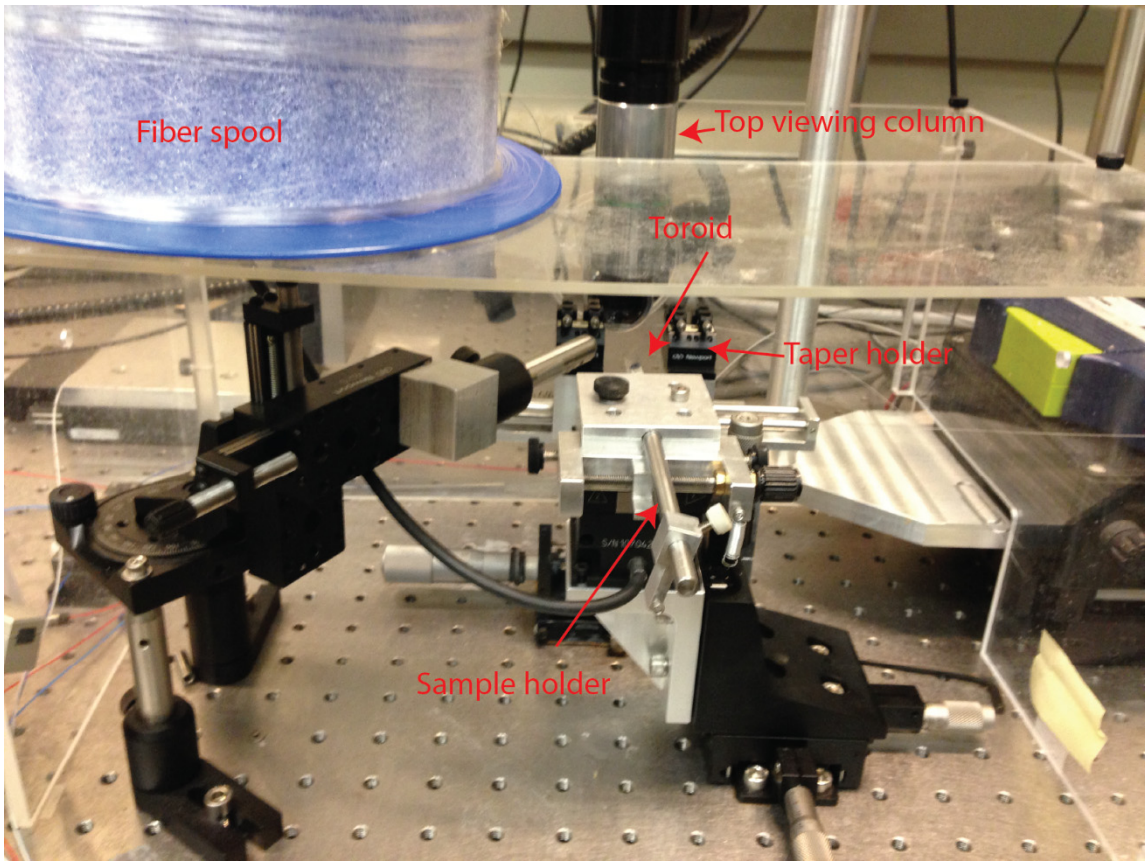

Supplementary Figure S1
Photograph of experimental setup.

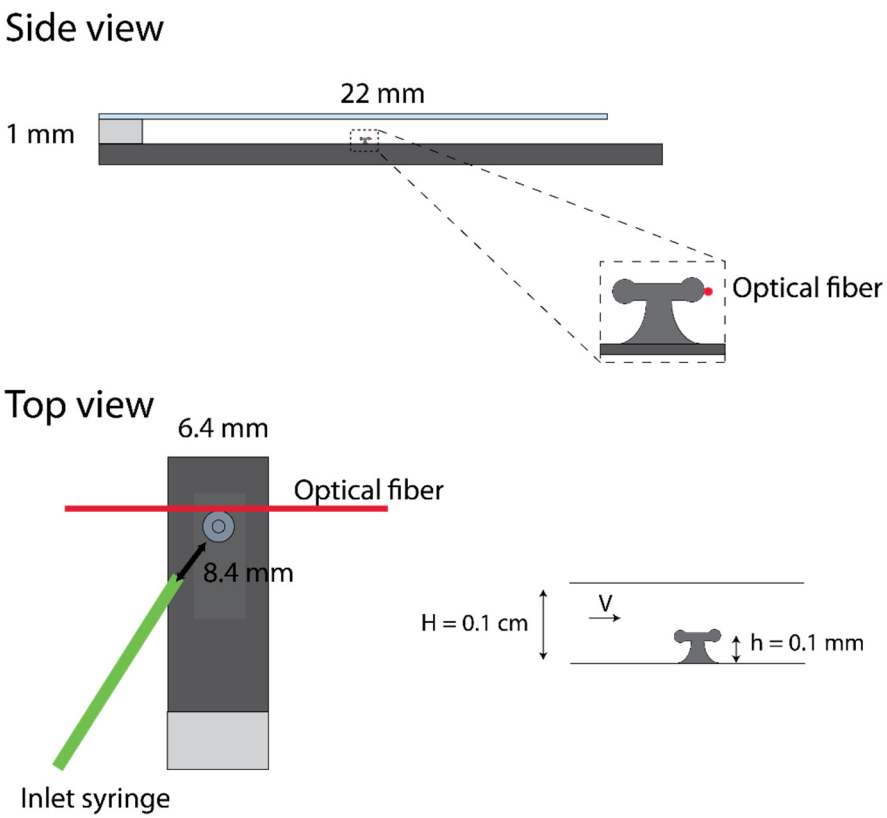

Supplementary Figure S2
Experimental schematic of microtoroid sample chamber with dimensions. The microtoroid is mounted on a steel base and a glass coverslip is placed on top. A portion of a microscope slide is used a spacer. The sample chamber is left open to allow for the optical fiber to pass through. *V* is the injection velocity, *h* is the height of the microtoroid and *H* is the height of the sample chamber.

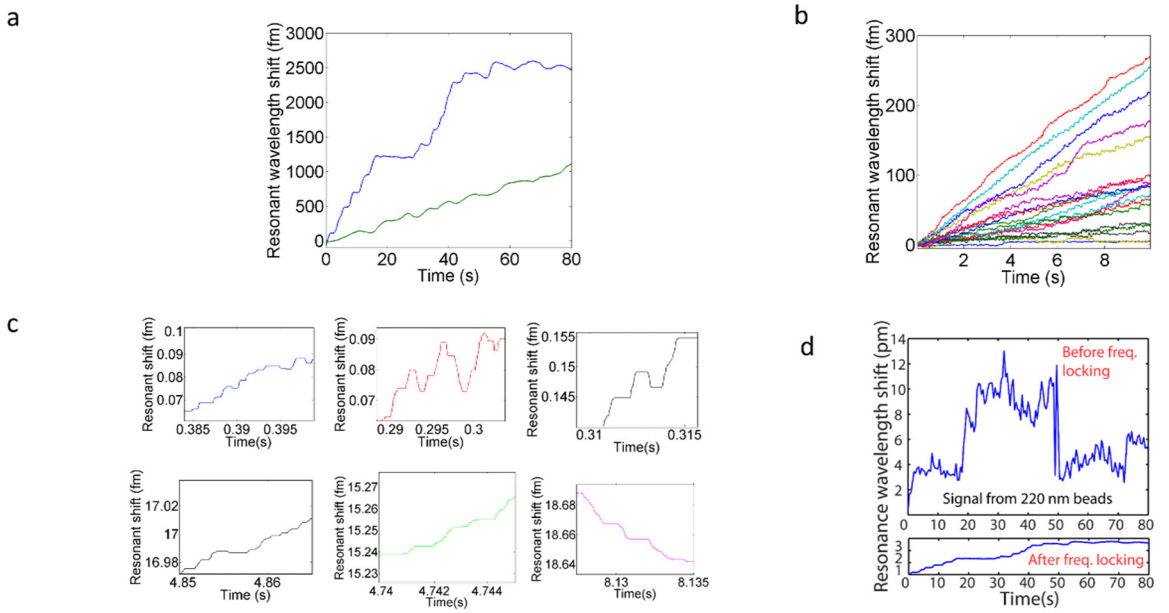

Supplementary Figure S3

Nanoparticle detection data for 2.5, 20, and 100 nm radius nanoparticles**.** Additional 10 nm radius nanoparticle data is shown in **Supplementary Fig. S4. (a)** Zoom-in of resonant wavelength shift over time of the microtoroid as 100 nm radius polystyrene latex nanoparticles bind to the microtoroid's surface. Each trace represents an experiment performed on a different toroid. **(b)** Zoom-in of resonant wavelength shift over time of the microtoroid as 20 nm radius polystyrene latex nanoparticles bind to the microtoroid's surface. The data presented here is of repeated injections on the same toroid. Two data points represent a repeated injection on a second toroid. **(c)** Zoom-in of resonant wavelength shift over time of the microtoroid as 2.5 nm radius silica nanoparticles bind to the microtoroid's surface. This represents data from two different toroids. **(d)** (top) Signal from a 110 nm radius nanoparticle solution without frequency locking has a noise level higher than signal. The apparent steps in this trace are too large to be single 110 nm radius nanoparticle, and are likely experimental or electronic noise (bottom) 100 nm radius nanoparticle detection experiment performed using frequency locking. The noise is essentially invisible when plotted on the same axis scale.

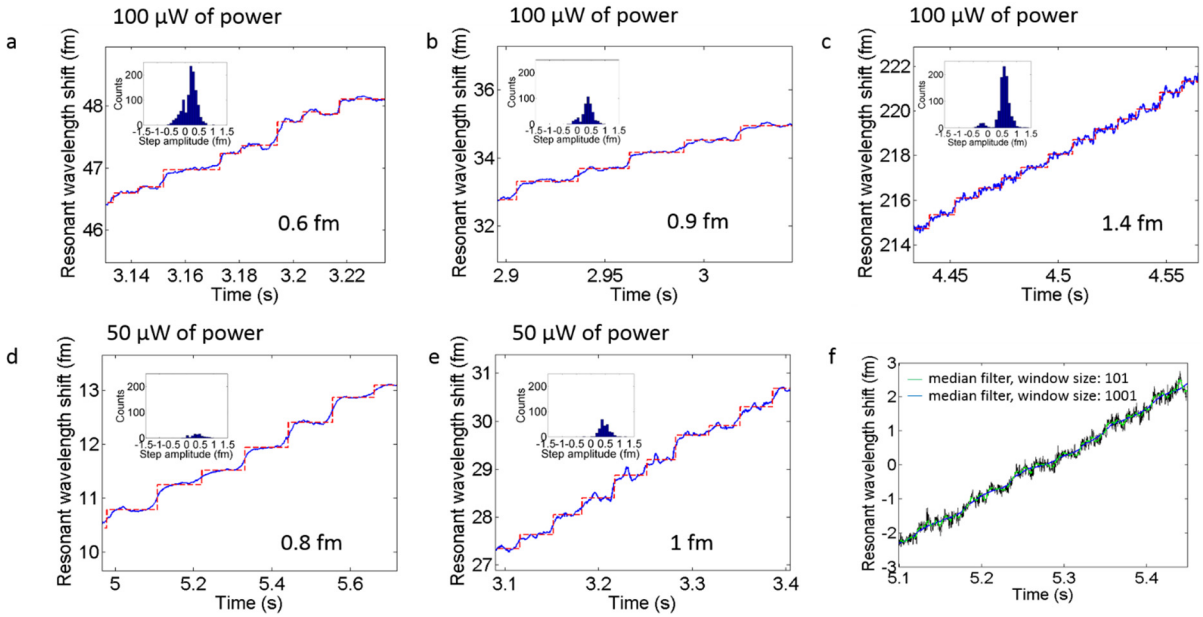

Supplementary Figure S4

10 nm radius nanoparticle detection by the microtoroid at different input coupling powers shows no detectable difference in step amplitude. **(a)-(c)** Zoom-in of 10 nm radius nanoparticle detection experiments performed at 100 µW of input power. The resonant wavelength shift over time of the microtoroid as the nanoparticles bind to the microtoroid's surface is shown in blue. The step-fit is shown as a red dashed line. The insets show histograms of the step amplitude. The maximum step amplitude is reported in the lower right hand corner of each graph. **(d)-(e)** Zoom-in of 10 nm radius nanoparticle detection experiments performed at 50 µW of input power. The resonant wavelength shift over time of the microtoroid as the nanoparticles bind to the microtoroid's surface is shown in blue. The step-fit is shown as a red dashed line. The insets show histograms of the step amplitude. No observable difference in step amplitude was noticed between the two different powers. For consistency, a median filter window size of 1001 was used in all experiments throughout the paper, however, for visualization purposes in (a), (b), (c), and (e), median window filter sizes of 101, 101, 101, and 11, respectively were chosen. This does not significantly alter found step heights and locations but was done because for these specific cases due to differences in arrival times of the nanoparticles, a median widow size of 1001 tends creates an overly rounded step-appearance (f). **(f)** Data from (e), (shown in black) plotted with a median window filter size of 101 (green) and a median window filter size of 1001 (blue). Increasing the median window filter size to 1001 does not alter the step height and location, but creates an overly rounded appearance. These experiments were performed on the same microtoroid.

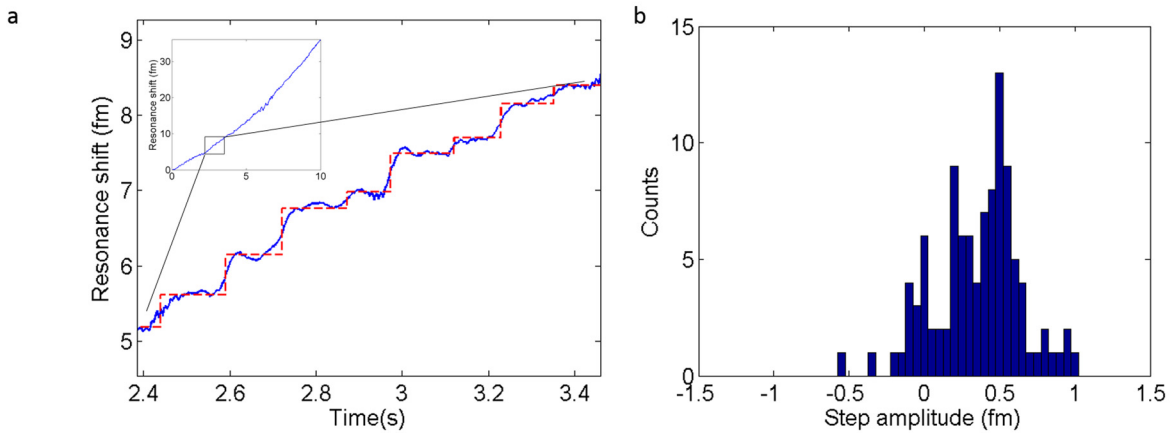

Supplementary Figure S5

Individual yeast ribosome (~12.5 nm radius) detection. **(a)** Zoom in of the resonant wavelength shift (blue trace) over time of the microtoroid as ribosomes bind to the microtoroid's surface. The step-fit is shown superimposed as a red dashed line. This is a similar but different data set than is shown in Figure 5. (inset) Zoom-out of the toroid response over the full recording range of 10 seconds. **(b)** Histogram of step amplitudes. The histogram bar seen at step sizes at around zero (no step) corresponds to small steps, whose sizes are not exactly zero.

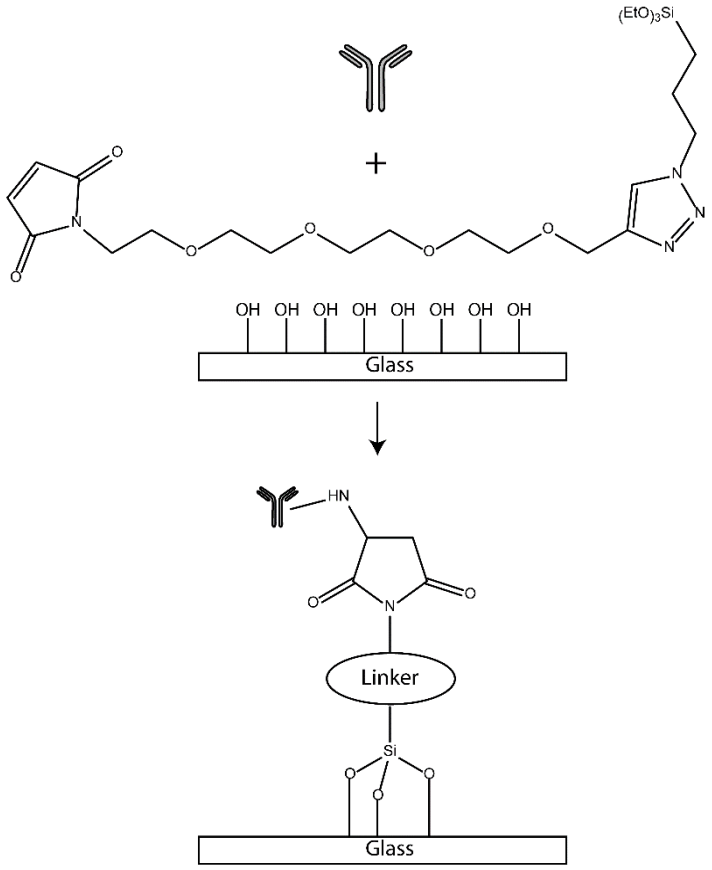

Supplementary Figure S6
Schematic demonstrating how the toroid's surface is sensitized for biological detection. A silane-PEG-maleimide linker (custom synthesis) is covalently bound to the surface of the toroid (represented as a glass substrate). Antibodies bind to the maleimide portion of the linker allowing for the selective detection of biological elements.

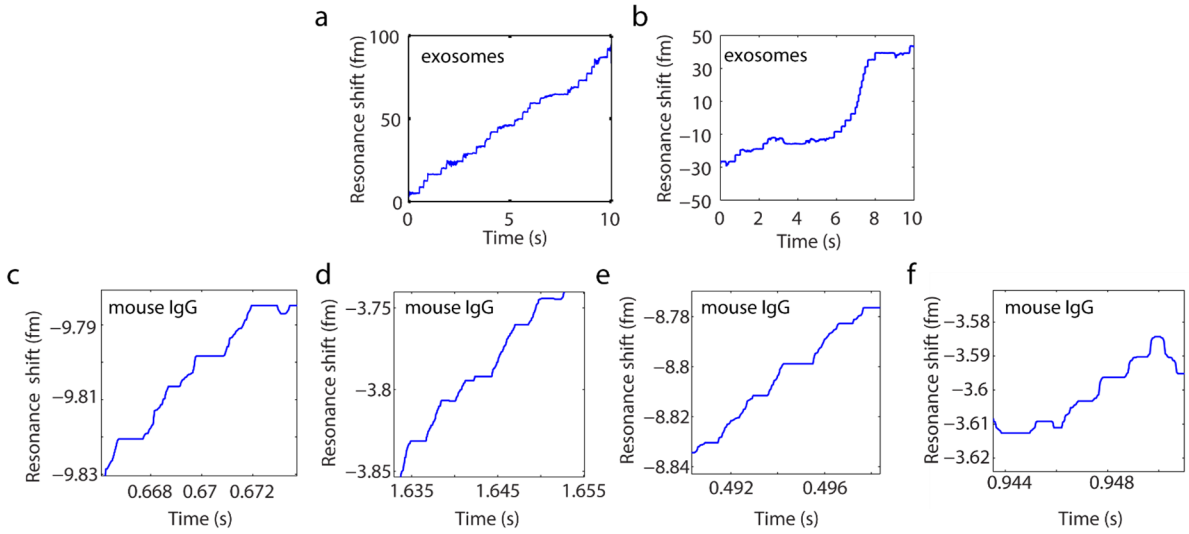

Supplementary Figure S7

Exosome and mouse IgG bioparticle detection data **(a)-(b)** Exosome detection recorded from two different experiments. As exosomes bind to the microtoroid's surface, the resonant wavelength of the microtoroid shifts as shown in the blue trace. Toroids were functionalized with the antibody CD-81. **(c)-(f)** Zoom-in of Mouse IgG detection data from four different experiments. As expected, the step amplitudes for the IgG detection are much smaller than for the exosome detection.

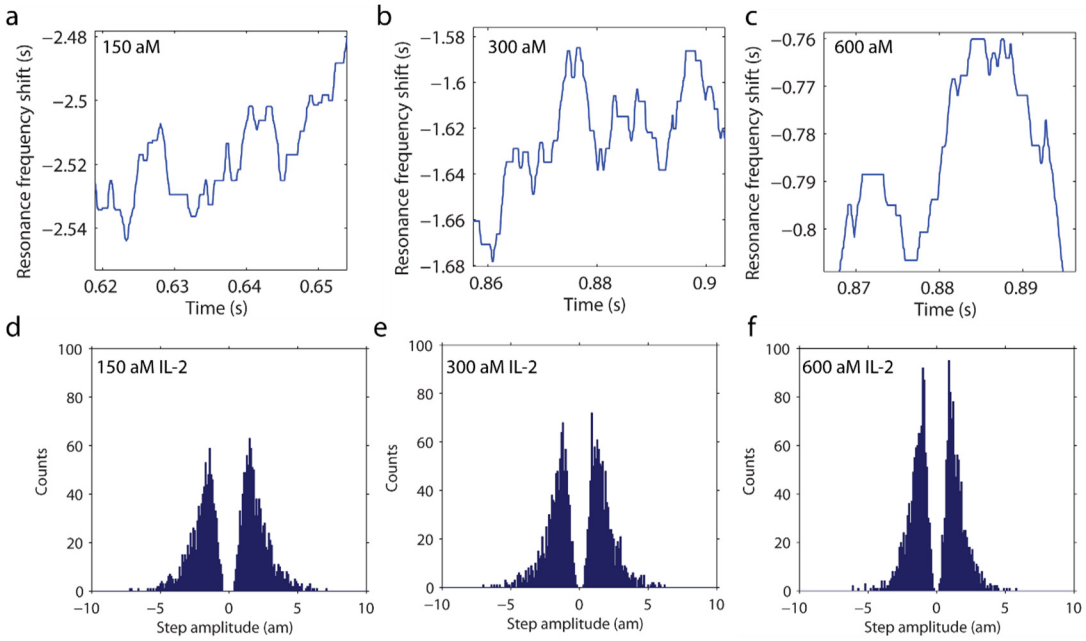

Supplementary Figure S8

IL-2 detection data at three different concentrations **(a)-(c)** Zoom-in of IL-2 step traces. Shown in blue is the resonance wavelength shift over time of the microtoroid as molecules bind to the microtoroid's surface. **(d)-(f)** Corresponding step amplitude histograms for **(a)-(c)**. As the concentration increases, the total number of particles increases in a linear fashion.

Theory

$$(\Delta\lambda)_{\max} = \frac{Da^3\left[E_0^2(r_e)/E^2{}_{\max}\right]}{2V_m}\lambda, \quad (1)$$

The wavelength shift upon particle binding depends on where on the resonator the particle lands. The largest wavelength shift ($\Delta\lambda_{max}$) occurs for particles binding at the equator of the microtoroid where the electric field is the largest. The amplitude of this shift is related to the size of the radius (*a*) of the bound particle through Eq. (1) [1]. In Equation (1), *D* is a dielectric factor calculated from the index of refraction of the particle and its surrounding media, λ is the wavelength of the laser, V_m is the volume of the electromagnetic field (mode) within the toroid, and $E_0^2(r_e)/E^2{}_{\max}$ represents the ratio of the intensity at the toroid's surface where the particle binds over the maximum intensity within the cavity. Both V_m and $E_0^2(r_e)/E^2{}_{\max}$ are calculated from finite element simulations (**Supplementary Figure S9**) and are found to be 330 μm^3 and 1/5.5, respectively.

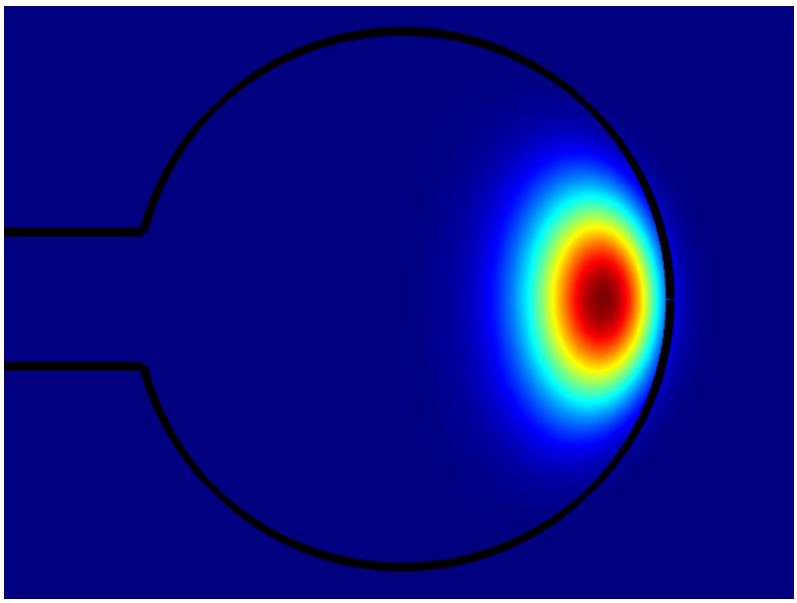

Supplementary Figure S9
COMSOL simulation of the capacitive Poynting energy density inside a silica microtoroid with major and minor diameter of 90 and 4 microns, respectively. The view presented is of a cross-section of the microtoroid. The toroid is immersed in water and has an azimuthal mode number of 662. The ratio of the maximum intensity inside the microtoroid to the intensity at the surface was found to be 5.5.

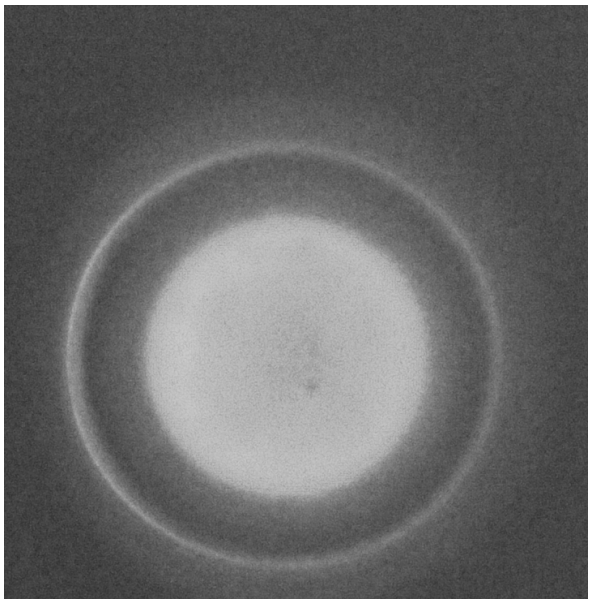

Supplementary Figure S10
Fluorescent image of FITC-Fc antibody fragments bound to the linkers on the surface of the microtoroid (top view, 40x magnification). Antibodies appear uniformly distributed around the rim of the microtoroid.

Explanation for an increase in the number of unbinding events observed for smaller particles

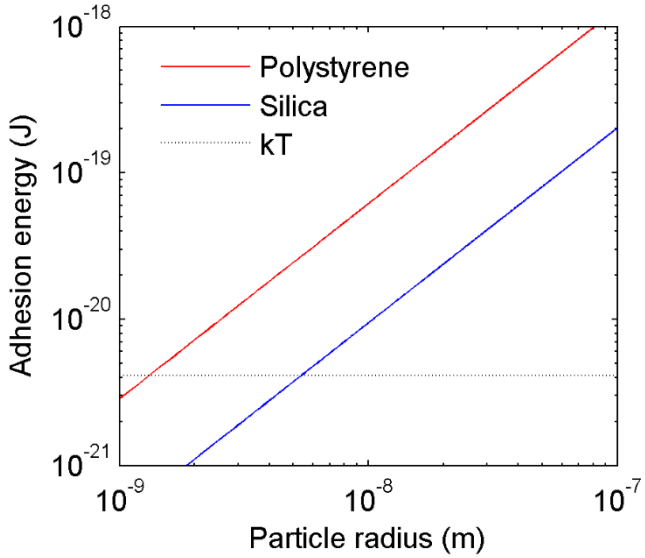

Supplementary Figure S11
Comparison between adhesion energy and thermal forces. For silica particle sizes below ~6 nm in radius, adhesion energy forces are of the same order of magnitude or smaller than kT, making unbinding events likely.

We estimate the adhesion energy based on the van der Waals attraction between the particle and the toroid as well as the particle's elastic modulus. As shown in Supplementary Figure S11, for polystyrene particles larger than ~9 nm in radius, the adhesion energy is more than an order of magnitude larger than kT, and therefore random thermal fluctuations are not likely to induce unbinding events. However, for silica particles smaller than ~6 nm in radius, the adhesion energy is of the same order or smaller than kT and therefore thermal fluctuations are likely to induce unbinding events. These theoretical estimates precisely agree with our experimental results, where the 10 nm radius polystyrene beads do not show many down-steps, while the 2.5 nm radius silica beads, and the even smaller IL-2 molecules, show many down-steps.

From [2], the total adhesion energy of two elastically deformable surfaces in equilibrium contact is given by:

$$E_0 = -0.6\,\pi\,a_0^2\,W = -1.2\,\pi\,a_0^2\,\gamma,$$

where a_0 is the contact area given by,

$$a_0 = \left(\frac{6\pi R^2 W}{K}\right)^{1/3},$$

W is the surface energy defined as 2γ, K is the elastic modulus, R is the particle radius, and $\gamma \cong A/24\pi(0.165\ nm)^2$, where A is the Hamaker constant for the material system.

This gives, $E_0 = -0.6\pi^{\frac{5}{3}} W^{\frac{5}{3}} \left(\frac{6}{K}\right)^{\frac{2}{3}} R^{\frac{4}{3}}$, which is plotted in Supplementary Figure S11 for both silica and polystyrene. The parameter values we use are:

K_{PS} = 3 GPa, where *PS* = polystyrene
$K_{\mathrm{SiO_2}}$= 50 GPa,
$A_{SiO_2-H_2O-SiO_2} \sim 10^{-20} J$
$A_{PS-H_2O-SiO2} \sim 10^{-20} J$

References

[1] Arnold, S., Khoshsima, M., Teraoka, I., Holler, S. & Vollmer, F. Shift of whispering-gallery modes in microspheres by protein adsorption. *Opt. Lett.* **28**, 272-274 (2003).

[2] Israelachvili, J.N. Intermolecular and surface forces, Edn. 3rd. (Academic Press, Burlington, MA; 2011).